Monthly Notices of the ROYAL ASTRONOMICAL SOCIETY
MNRAS **517,** 1483–1490 (2022) https://doi.org/10.1093/mnras/stac2427

Explosion imminent: the appearance of red supergiants at the point of core-collapse

Ben Davies,[1]★ Bertrand Plez[2] and Mike Petrault[2]

[1]*Astrophysics Research Institute, Liverpool John Moores University, Liverpool Science Park IC2, MV 146 Brownlow Hill, Liverpool L3 5RF, UK*
[2]*Laboratoire Univers et Particules de Montpellier, Université de Montpellier, CNRS, F-34090 Montpellier, France*

Accepted 2022 August 19. Received 2022 August 19; in original form 2022 April 22

ABSTRACT

From the early radiation of type II-P supernovae (SNe), it has been claimed that the majority of their red supergiant (RSG) progenitors are enshrouded by large amounts of circumstellar material (CSM) at the point of explosion. The inferred density of this CSM is orders of magnitude above that seen around RSGs in the field, and is therefore indicative of a short phase of elevated mass-loss prior to explosion. It is not known over what time-scale this material gets there: is it formed over several decades by a 'superwind' with mass-loss rate $\dot{M} \sim 10^{-3}\,\mathrm{M}_{\odot}\,\mathrm{yr}^{-1}$; or is it formed in less than a year by a brief 'outburst' with $\dot{M} \sim 10^{-1}\,\mathrm{M}_{\odot}\,\mathrm{yr}^{-1}$? In this paper, we simulate spectra for RSGs undergoing such mass-loss events, and demonstrate that in either scenario, the CSM suppresses the optical flux by over a factor of 100, and that of the near-IR by a factor of 10. We argue that the 'superwind' model can be excluded as it causes the progenitor to be heavily obscured for decades before explosion, and is strongly at odds with observations of II-P progenitors taken within 10 yr of core-collapse. Instead, our results favour abrupt outbursts < 1 yr before explosion as the explanation for the early optical radiation of II-P SNe. We therefore predict that RSGs will undergo dramatic photometric variability in the optical and infrared in the weeks-to-months before core-collapse.

Key words: circumstellar matter – stars: evolution – stars: late-type – stars: massive – supergiants – supernovae: general.

1 INTRODUCTION

For the few dozen II-P supernovae (SNe) that have occured within 30 Mpc, it has been possible to identify the progenitor star in high-resolution imaging taken 1–10 yr before it exploded. In the cases where a progenitor is identified, the star is always inferred to be both luminous ($>10^{4.5}\,\mathrm{L}_{\odot}$) and with colours consistent with spectral type M (Smartt et al. 2004, 2009; Smartt 2015; Davies & Beasor 2018, 2020). This evidence therefore strongly points towards red supergiants (RSGs) as being the direct progenitors for the most common type of core-collapse SN.

Whilst pre-explosion imaging can tell us what the star looked like within a decade of the SN, the SN radiation itself can give us hints about what the star looked like at the moment the core collapsed. In particular, in the first few days after core-collapse as the explosion 'breaks out' of the star's optically thick surface layers, we may learn about the physical conditions at the star's upper atmosphere and inner circumstellar material (CSM). Spectroscopy taken within a day or so of shock breakout reveal narrow emission lines which originate in the dense CSM, but which disappear quickly as the CSM is overrun by the blast-wave (e.g. Yaron et al. 2017; Jacobson-Galán et al. 2022). In both works cited, analysis of this 'flash' spectroscopy has suggested circumstellar densities of between 10^{-13} to $10^{-14}\,\mathrm{g\,cm}^{-3}$ at a few $\times\,10^{14}$ cm, which is orders of magnitude more dense than, for example, the CSM around Betelgeuse (Harper, Brown & Lim 2001). Subsequent similar studies of larger samples of SNe find that the fraction of objects demonstrating this behaviour increases the closer the SN is observed to explosion (Khazov et al. 2016; Bruch et al. 2021). Indeed, the latter study found 6 out of 10 objects observed within 2 d displayed flash-ionized spectral features. This hints that perhaps the majority of II-P SNe might exhibit this evidence for dense CSM around the progenitor as long as they are observed early enough.

Corroborating evidence for dense CSM around II-P progenitors comes from their early-time light curves. If the CSM is optically thick, it delays the breakout of the shock, allowing the explosion to cool further before it emerges. This leads to a shorter time-scale for the SN radiation to shift into the optical bands, causing sharper rise-times in the optical light curve (Moriya et al. 2017; Morozova, Piro & Valenti 2017). Hydrodynamical modelling of the early optical light curve, and the steepness of the initial rise, can then be used to estimate the radius/density of the shock breakout location. Early work on single SNe indicated densities $>10^{-10}\,\mathrm{g\,cm}^{-3}$ within $\sim 0.5 R_{\star}$ of the stellar surface (Dessart, John Hillier & Audit 2017; Moriya et al. 2017; Morozova et al. 2017). These densities are many orders of magnitude higher than those inferred around typical RSGs, or even RSGs with very high mass-loss rates (see fig. 1 of Davies & Plez 2021). Later work on larger samples of objects suggests that evidence for dense CSM is seen around 70–90 per cent of II-P SNe studied (Förster et al. 2018; Morozova, Piro & Valenti 2018).

The open question now is how this pre-SN CSM was formed, and a clue to answering this question will come from establishing over what time-scale the CSM forms. The models put forward to explain

★ E-mail: b.davies@ljmu.ac.uk

this existence of the CSM fall into roughly two camps, which we will refer to as the 'outburst' and 'superwind' scenarios. Each of these scenarios will be discussed in more detail in Section 2, but briefly they can be differentiated by the time-scale over which they form the CSM. In the 'outburst' scenario, the CSM is the product of a very high mass-loss rate event ($\dot{M} \sim 0.1\,\mathrm{M}_\odot\,\mathrm{yr}^{-1}$) lasting of the order of a year (e.g. Morozova et al. 2018). In the 'superwind' scenario, the CSM is the product of a steady-state outflow with a very high mass-loss rate, which operates for $\gtrsim$100 yr prior to explosion (e.g. Förster et al. 2018). A third possibility is discussed in Dessart et al. (2017), in which the atmospheric scale-height is puffed up by factors of 10 to 30, with a wind stitched on top. These models generally have lower CSM masses than the 'superwind' or 'outburst' models, but have greater CSM densities within $\sim 2R_\star$ ($\times 10^{3-5}$ higher than typical RSGs). No time-scale for the generation of the CSM is provided for this latter scenario.

Hydrodynamical modelling of the SN's early-time light curve alone is not capable of discriminating between the two scenarios. However, since each scenario makes a different predictions about how the progenitor star should look in the years before SN, they can be contrasted by simulating how the progenitor should look in the decade or so before explosion. In this paper, we will construct models replicating each scenario[1] (Section 2), and use them to compute synthetic spectra for each of the two scenarios described above (Section 3). We will then compare our results to observations of progenitors in the literature (Section 4). We conclude in Section 5.

2 DESCRIPTION OF PRE-SN MODELS

2.1 'Outburst' models

For the 'outburst' model, we refer to the work of Morozova et al. (2017, 2018, 2020, the latter two papers hereafter referred to as M18 and M20). In M18, it was argued that the early-time light curves of a sample of SNe suggested that in the majority of cases, an excess of 0.1 $\mathrm{M}_\odot$ of CSM was confined within $\sim 10^{14}$ cm, which is approximately $2R_\star$ for a typical RSG. To achieve this mass of CSM, these authors suggested that a wind of mass-loss rate $\dot{M} \sim 0.1\,\mathrm{M}_\odot\,\mathrm{yr}^{-1}$ (for a putative wind speed of 10 $\mathrm{km\,s}^{-1}$) would be required. Such mass-loss rates are far many orders of magnitude above those of typical massive star winds, and are associated more with eruptive outbursts (e.g. η Car) rather than quiescent winds. The sheer scale of such outbursts suggests that they would require a large, subsurface energy deposition rather than be opacity-driven as in a normal massive star wind.

In a follow-up paper, M20 suggested a potential source of such an energy release could be wave-heating associated with late-stage nuclear burning. To simulate such an event, these authors took the pre-SN 15-$\mathrm{M}_\odot$ model of Sukhbold, Woosley & Heger (2018), manually deposited between $10^{46}-10^{47}$ erg of energy at the base of the convective envelope, and computed the evolution of the stellar structure as the shockwave propagated outwards through the envelope. Once the shock had reached the surface (which we define in this study as the beginning of the 'outburst') and expanded the outer layers, M20 took a number of models at different time-steps, manually exploded them, and computed the resulting light curve. The conclusion of the paper was that the light curves of II-P SNe were best matched by outbursts which pierce the stellar surface $\sim$160 d before explosion, at which time around 1 $\mathrm{M}_\odot$ of CSM has built up at radii above the original photosphere.

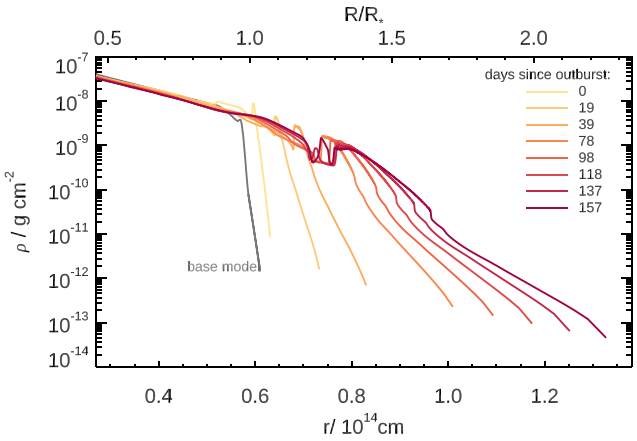

Figure 1. Density profiles of the outburst models of M20 as a function of time since the shockwave pierced the progenitor surface, which we define here as day 0 (defined as day 140 in M20). The last model, at 157 d since the emergence of the outburst, is that determined by to be the best-fitting pre-explosion density profile.

The density profiles as a function of time after the shock has penetrated the stellar surface are shown in Fig. 1.[2] If we define the circumstellar mass M_{CSM} as that mass located above the original progenitor surface, the mass at +160 d is extremely high – over 1 $\mathrm{M}_\odot$, an order of magnitude above those inferred in M18. To generate this much CSM in such a short time, this implies mass flow rates $>1\,\mathrm{M}_\odot\,\mathrm{yr}^{-1}$.

2.2 'Superwind' models

In Moriya et al. (2017), it was first suggested that a wind with a mass-loss rate orders of magnitude below that inferred by Morozova et al. (2016) may also be able to explain the early-time SN radiation, provided the wind had an extended acceleration zone. At fixed $\dot{M}$, the circumstellar density is inversely proportional to the outflow speed, and so a wind that expands very slowly until it reaches large radii will be much more dense in the inner regions. Thus, a slowly-accelerating wind with a much lower $\dot{M}$ may have the same CSM density in the inner wind as a higher $\dot{M}$ outburst which is accelerated more steeply.

However, even with such a shallow acceleration zone, mass-loss rates of the order of $10^{-3}\,\mathrm{M}_\odot\,\mathrm{yr}^{-1}$ are still required: orders of magnitude larger than those of typical RSGs, and a factor of $\sim$100 higher than even the most extreme objects (e.g. Beasor & Davies 2018; Beasor et al. 2020; Humphreys et al. 2020). Furthermore, with a much reduced $\dot{M}$ with respect to the 'outburst' scenario, such a wind would need to operate for 100 s of years prior to SN in order to build up the CSM necessary to reproduce the early-time light curves (cf. 100 s of days for the 'outburst' model).

[1] Dessart et al. (2017) do not provide time-scales for how long it takes to generate the CSM in their models, so at this time we do not explore these models' synthetic spectra. In this paper, we investigate only the Förster et al. (2018) and Morozova et al. (2020) models.

[2] We define day 0 as the first model in which the outburst has pierced the stellar surface. This is 140 d after the energy was deposited at the base of the convective envelope, and so this model is defined as day 140 in M20.

2.2.1 *Construction of the 'superwind' models*

Following Davies & Plez (2021), for our base model, we begin with an MARCS model atmosphere of effective temperature $T_{\rm eff} = 3800$ K, gravity $\log g = 0.0$, Solar-scaled abundances, and microturbulence $\xi = 4\,{\rm km\,s^{-1}}$.[3] The luminosity $L = 10^5\,{\rm L_\odot}$, and the radius $R_\star = 730\,{\rm R_\odot}$. To this atmosphere, we add a nominal ambient wind with $\dot{M} = 10^{-7}\,{\rm M_\odot\,yr^{-1}}$, following the same procedure as Davies & Plez (2021).

To this base model, we add CSM with a density profile ρ varying with radius r according to the mass continuity equation

$$\dot{M} = 4\pi r^2 \rho(r) v(r), \tag{1}$$

where v is the outflow speed. Following Förster et al. (2018, hereafter referred to as F18), we parametrize $v(r)$ as a beta-law

$$v(r) = v_0 + (v_\infty - v_0)\left(1 - \frac{R_\star}{r}\right)^\beta, \tag{2}$$

where β dictates the steepness of the acceleration, v_∞ is the terminal wind velocity, and v_0 is the initial speed of the wind at the photosphere which must be non-zero to avoid the density tending to infinity at small r. Following F18, we adopt $\dot{M} = 10^{-3}\,{\rm M_\odot\,yr^{-1}}$, $\beta = 3$, $v_\infty = 10\,{\rm km\,s^{-1}}$, and a value of $v_0 = 0.0125\,{\rm km\,s^{-1}}$ is chosen to ensure that the density at the inner wind knits continuously with that at the outer photosphere at the location where $T(r) = T_{\rm eff}$. As with F18, the wind is propagated out to a distance $r_{\rm wind} = 20R_\star$, though we compute a series of models at shorter $r_{\rm wind}$ to study the spectral evolution of the star throughout the launching of the wind (see Fig. 2).

To compute the emerging flux through the wind, we must also specify a temperature profile $T(r)$. To compute $T(r)$, in this work we make the assumption that radiative equilibrium holds at all depths in the wind. To do this, we begin with the T profile of the MARCS model, and at the point the wind meets the atmosphere we make the initial estimate of T scaling as $r^{-0.5}$ from the inner to the outer extent of the wind. We then iterate on the T-structure to ensure that at every depth in the wind the condition

$$\int_{\lambda_1}^{\lambda_2} \kappa_\lambda (J_\lambda - B_\lambda) {\rm d}\lambda = 0, \tag{3}$$

is satisfied. Here, κ_λ, J_λ, and B_λ are the opacity, the intensity of the radiation field, and the Planck function, respectively. To do this, we use TURBOSPECTRUM V19.1 to solve the radiative transfer equation between $\lambda_1 = 0.2\,\mu$m and $\lambda_2 = 12\,\mu$m, at wavelength sampling of $\lambda/\Delta\lambda = 500$, and determine κ_λ, J_λ, and B_λ at all wavelengths and all depths. The wavelength limits λ_1 and λ_2 are chosen to encompass > 95 per cent of the flux at all temperatures < 6000 K, which is the majority of the atmosphere and wind. In practice, iterating the T-structure results in very little shift from the initial estimated profile for those models where the superwind has yet to reach $2R_\star$. For later models, a very small adjustment to the temperature profile was necessary, where $T(r/R_\star > 2)$ had to be reduced by a few per cent. After a small number of iterations, the luminosity at every depth was consistent to within 5 per cent, and the luminosity at the outer and inner radii are consistent to within 0.05 dex. Furthermore, very little change to the emergent spectrum was seen between the iterated and initial models.

[3]As we will see later, the details of the stellar atmosphere are relatively unimportant as it is almost completely masked by the CSM.

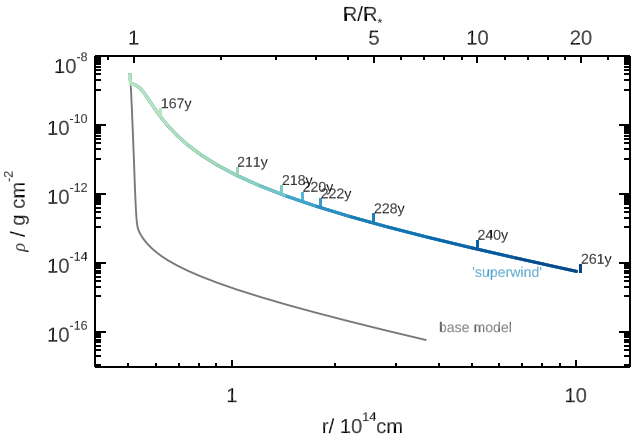

Figure 2. Density profile of the 'superwind' model. The extent of the superwind's outer radius as a function of years since its initiation is indicated by the data labels.

2.3 Computing the synthetic spectra

To compute the emergent spectra of these models, we take the density and temperature profiles at each stage of the simulation for each of the two scenarios, and pass them through our modified version of TURBOSPECTRUM (Plez 2012; Davies & Plez 2021). The code solves for the molecular equilibrium in the cooler layers, and computes the radiative transfer through the atmosphere under the assumption of local thermodynamic equilibrium. We assume Solar metallicity and Solar-scaled abundances in all spectra, noting that RSGs may display surface abundances consistent with mild CNO processing (Davies et al. 2009). Though we do not know quantitatively what the impact of these approximations are, as we will see in the next section, the strengths of the molecular features are enormous, far beyond that seen in 'normal' RSGs. Therefore, our conclusions are robust to these approximations provided they do not cause the TiO and ZrO band strengths to decrease by more than a factor of $\sim$5, such is the effect on the progenitor colours (see Section 4).

3 RESULTS

The synthesized spectra for the two scenarios are plotted in Figs 3 and 4, along with a 3800-K MARCS model which was the progenitor. All spectra have been smoothed to a constant resolving power of $R \equiv \lambda/\Delta\lambda = 1000$ to make the spectral behaviour clearer around the molecular bands.

The time evolution of various physical properties and observables during the pre-SN events are illustrated in Figs 5 and 6. In each of these plots, the time-dependent photospheric radius $R_{\rm phot}$ (second-top panel in each figure) is defined as the flux-weighted average of the $\tau_\lambda = 1$ surface. The circumstellar mass $M_{\rm CSM}$ is defined as the mass above the *original* progenitor photosphere.

Below, we discuss the results from each scenario in more detail.

3.1 'Outburst' spectra

The first model we compute is that shortly after the shockwave penetrates the surface layers, defined in M20 as $t = 140$ d, but defined here as $t = 0$. The star expands slightly, and temperature at the surface increases by about 1200 K, causing an increase in bolometric luminosity. The emergence of the shock leads to a 'thickening' of the outer layers, effectively reducing the atmosphere scale height.

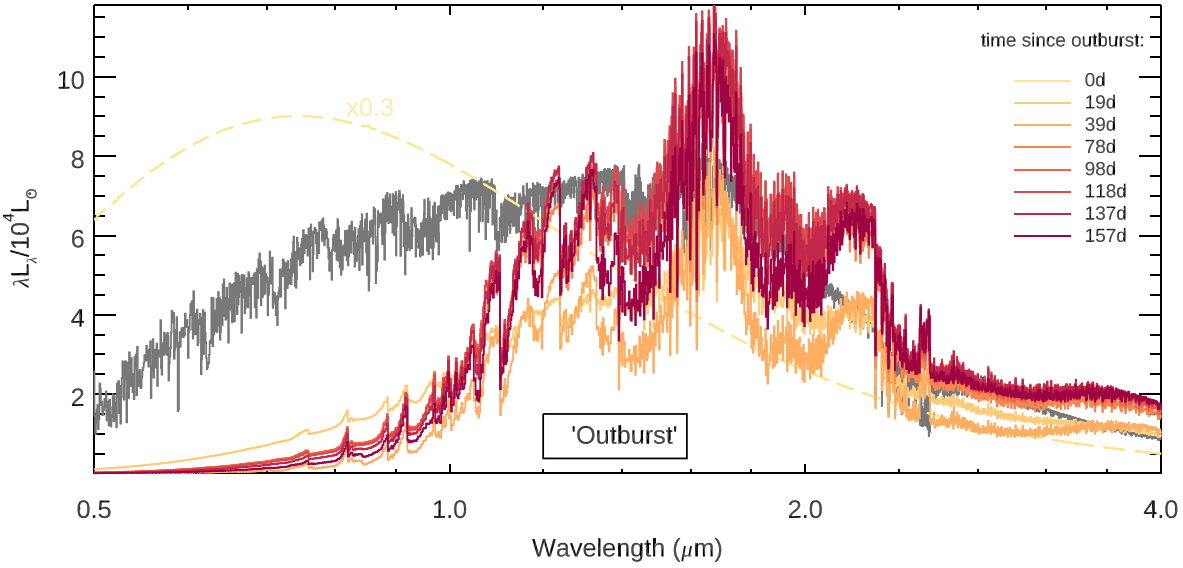

Figure 3. Simulated spectra of the outburst models, as a function of time since the initial outburst. All models have been smoothed to a constant resolving power of $\lambda/\Delta\lambda = 1000$. The earliest model has been scaled down by a factor of 0.3 for clarity. The spectrum of the base model is shown in grey.

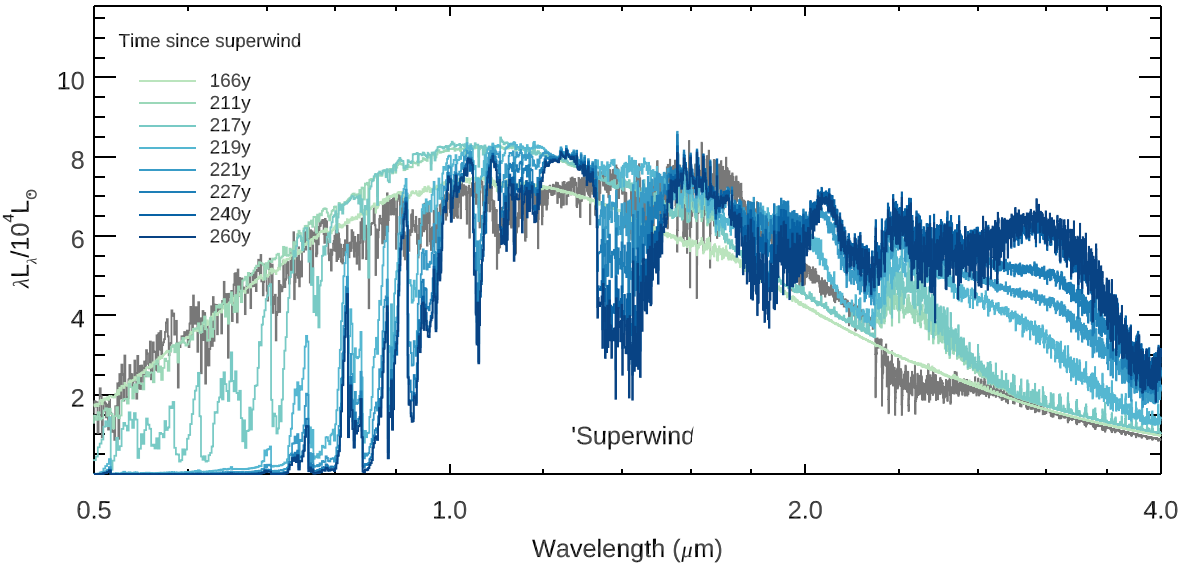

Figure 4. Simulated spectra of the 'superwind' models, once the wind has extended to the radii indicated by the legend. The spectrum of the base model is shown in grey.

These factors combined lead to a dramatic reduction in the molecular opacity, and an almost featureless spectrum aside from some weak atomic absorption that cannot be seen at the spectral resolution of Fig. 3 ($R = 1000$). In terms of the star's behaviour in colour–magnitude space, the star briefly becomes bluer and brighter in the *I*-band.

Only a few days after the shock breakout, the star surface cools to below the initial effective temperature, while the photosphere expands. Luminosity is not conserved during this time, and the star dims to become ∼0.3 dex fainter than the initial model. This cooling of the photospheric layers, combined with the atmosphere becoming more extended, leads to an increase in molecular opacity. The TiO and ZrO bands in the optical, as well as the CN, CO, and H_2O bands in the near-IR, all go into absorption. The cooler temperature, fainter luminosity, and increased molecular opacity lead to the star becoming ∼4 mag fainter in the *I*-band, and ∼2 mag redder in $R - I$, within a month of the breakout of the outburst. For the remaining ∼100 d of the simulation, the outer layers continue to expand, forcing the photosphere to larger radii. The photospheric temperature decreases very slightly during this time, causing the bolometric luminosity to remain constant to within ∼0.1 dex, and the *R*- and *I*-band fluxes to be stable to within a few tenths of a magnitude. According to M20, the model that best reproduces the early-time SN spectrum is the last of this series, meaning that the putative SN would occur ∼160 d after the emergence of the pre-SN outburst, which is the dark red spectrum in Fig. 3 and the final data point in Fig. 5.

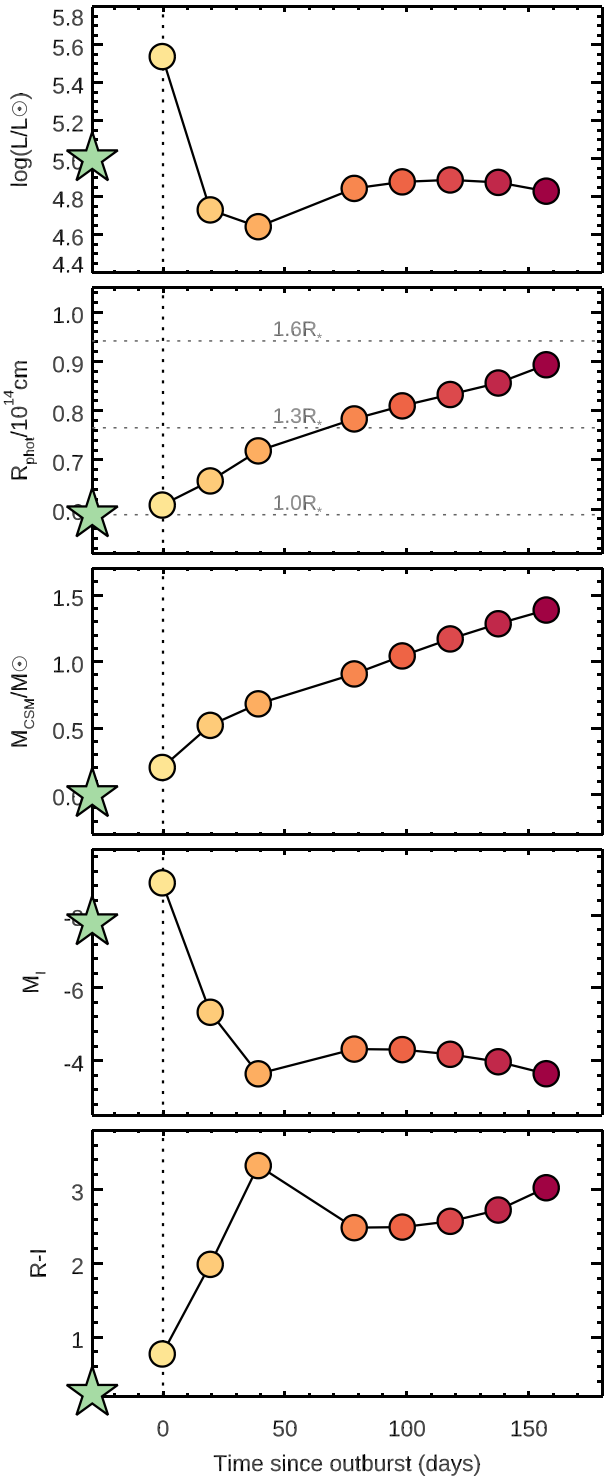

Figure 5. Evolution of the star's observables during the outburst. Top panel: bolometric luminosity; second top panel: the radius of the photosphere, defined as the flux-weighted average of the $R_\lambda(\tau = 1)$ surface; centre panel: circumstellar mass, defined as the mass now above the original photosphere; second bottom panel: absolute magnitude in the I-band; bottom panel: $R - I$ colour. The green star indicates the properties of the base model. The vertical dashed line indicates the time at which the subsurface eruption breaks the surface of the star, defined in M20 as $t = 140$ d, but defined here as $t = 0$.

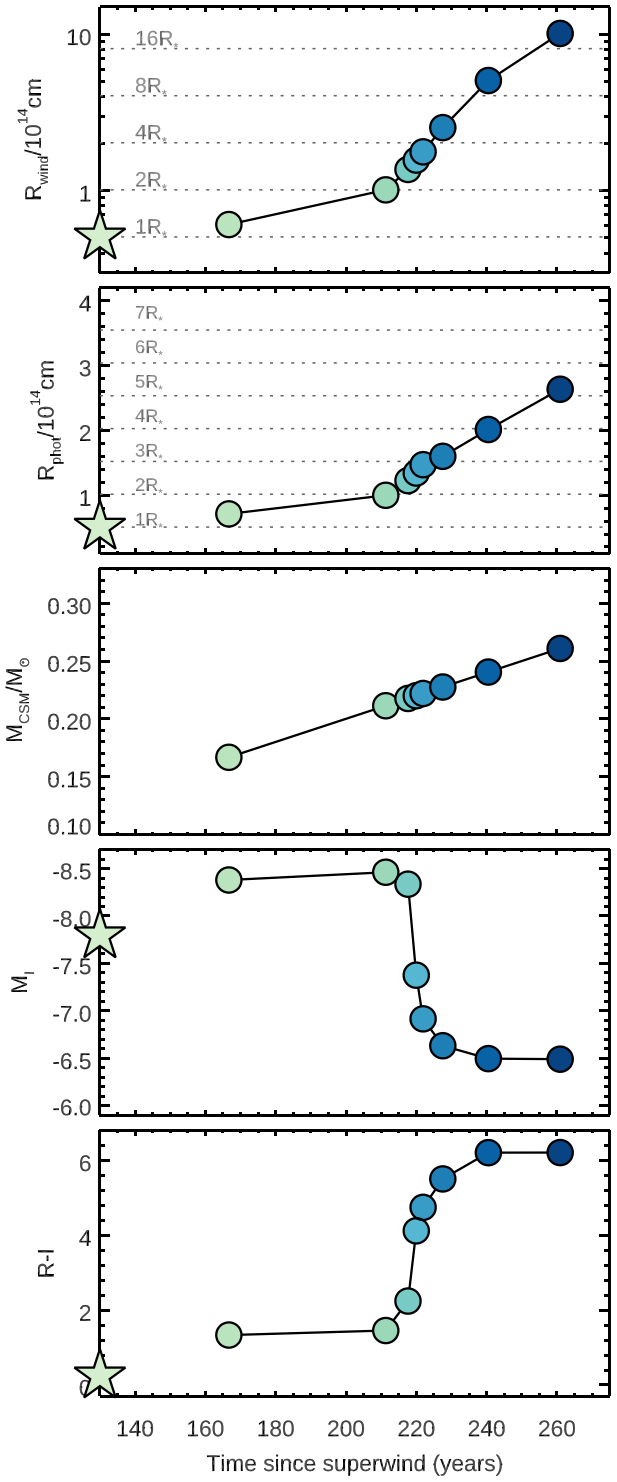

Figure 6. Evolution of observables during the superwind. The panels show the same as Fig. 5, apart from the top panel which in this figure illustrates the radius of the outermost part of the wind.

Under this scenario, we can conclude that the signature of an impending SN would be a very brief brightening of a few days, during which the star became bluer, followed by a dramatic dimming and reddening over the next month, with the star remaining in a similar state for several more months until SN.

3.2 'Superwind' spectra

During the first ∼160 yr, the very shallow acceleration profile of the wind (set by the high value of β) leads to the CSM to accumulating close to the initial photosphere, causing the atmosphere to 'thicken' as in the outburst scenario. As this happens, the continuum opacity increases, but the molecular line opacity stays roughly constant. The effect is to 'fill-in' the absorption lines, leading to an SED which has a similar overall shape but has less absorption features.

After ∼200 yr, the wind expands outwards beyond $2R_\star$, and we begin to see the first molecular features as the CO bands go into emission, but in terms of its brightness at R and I the star has changed only very little. Just after 220 yr, the outer 'superwind' reaches $3R_\star$, and here it approaches its maximum acceleration. It is at this point that we see the most dramatic change in the star's properties (see Fig. 6), as the outer wind is now beginning to expand at a rate close to its terminal velocity. The very high mass-loss rate causes the effective flux-averaged radius to move outwards, reaching $5R_\star$ after around 250 yr. During this time, the optical absorption bands of TiO and ZrO become heavily saturated, the CO and CN bands in the J and H bands also go into absorption, while the CO and H_2O bands >1.8 μm go into emission. This causes the star to become fainter in the I-band by ∼2 mag, but the most dramatic effect is seen in the star's $R-I$ colour which becomes ∼ 6 mag redder than the initial colour of the base model.

At $20R_\star$ (around 260 yr after the onset of the 'superwind'), the local temperature drops below 1000 K, at which point we would expect dust to form. Even the dustiest RSGs known, such as VY CMa or WOH G64 (e.g. Shenoy et al. 2016; Goldman et al. 2017) have mass-loss rates which are at least an order of magnitude below that of the superwind. Therefore, we would expect that once this star begins to form dust, it will do so on a scale beyond seen in any field RSG. This would result in the star becoming even fainter and redder than our predictions presented here.

The obvious aspect that differentiates this scenario from the 'outburst' is the time-scale involved. Whereas the time from outburst to SN is around 0.5 yr, by contrast the 'superwind' takes over 250 yr to reach $20R_\star$, which is the outer wind radius necessary to reproduce the observed features in the SN light curves (Moriya et al. 2017; Förster et al. 2018). By the time of explosion, our results indicate that the star would have been exceptionally red for >40 yr prior to core-collapse. The only way to make this CSM accumulate faster would be to increase $\dot{M}$ and decrease β, at which point the 'superwind' starts to become an analytic approximation of the 'outburst' described in M20.

4 COMPARISON TO OBSERVATIONS OF II-P PROGENITORS

To compare our results to observations, we use the sample of II-P SNe from nearby galaxies presented in Davies & Beasor (2020). This sample contains nearly all known II-P SNe with host galaxies within 30 Mpc between 1999 and 2017, and so can be assumed to be volume limited. The only biases present in this sample are (a) any SNe that may have occurred in low surface brightness galaxies would likely be missing, owing to their host galaxy lacking pre-explosion imaging; and (b) an SN in a very crowded region – namely SN 2016cok – is missing from our sample, as the progenitor is impossible to identify without very late time observations with which to perform image subtraction (see Kochanek et al. 2017).

To compare these SNe to our results, we begin with the subset of objects which have pre-explosion detections or upper limits in the *F*814*W* or *I*-band filters. For each of these objects, we determine the absolute *I*-band magnitudes from their pre-explosion photometry, their distance modulii, and extinction (Davies & Beasor 2018, 2020, and references therein). We also define the time before SN that each progenitor was observed as being the difference between the observation date and the SN discovery date. From this subset of progenitors, we next identify those objects which have colour information in the form of a related detection in the R (or *F*606*W*) band. The magnitudes and colours of the II-P progenitors as a function of the number of years before SN that they were observed are plotted in Fig. 7. In total, we have 12 events with pre-explosion *I*-band imaging, and six events with a constraint on $R-I$.[4]

On each panel of Fig. 7, we overplot the predicted time evolution of the two scenarios studied in the previous section. For the 'outburst', the SN time is assumed to be 160 d after the outburst; and in the 'superwind' model, it is taken to be 260 yr – the time at which the wind reaches $20R_\star$. For each scenario, the base input model was a 10^5 $L_\odot$ star with spectral type M0. The locations of this input star on these diagrams is marked in grey, as well as the locations of similar stars with different luminosity (in the left-hand panel only).

The first thing we note here is that no RSG SN progenitor has yet been observed *after* we would expect the outburst to have happened in the 'outburst' scenario. Though three SNe (03gd, 05cs, and 17eaw) were observed ∼200 d before explosion, which is roughly when the outburst would be expected, we are currently unable to rule out the 'outburst' scenario from these data.

However, we are able to make conclusive arguments regarding the 'superwind' scenario. Recall that in this scenario, the pre-explosion CSM accumulates slowly over several decades, causing the star to become a factor of 3 fainter in I and over 5 mag redder in $R-I>$ 40 yr before explosion. This is strongly contradicted by observations of nearby SNe.

In Fig. 7, we first see that none of the progenitors were as faint as we would expect a 10^5 $L_\odot$ progenitor with a superwind to be. Furthermore, of the four objects for which we have pre-explosion colours (right-hand panel of Fig. 7), three had colours of a normal M0 supergiant. The one outlier is 17eaw, which is still several magnitudes bluer than we would expect if it were experiencing a superwind; we discuss this object in more detail below. Zero out of four objects is obviously inconsistent with the conclusions of F18 that 92 per cent of II-P SNe progenitors experienced superwinds before they exploded. Formally, the probability that we would randomly find zero objects with superwinds in an unbiased sample of four progenitors, if the intrinsic fraction was 92 per cent (as reported in F18), is $p \simeq 5 \times 10^{-5}$.

4.1 The case of SN 2017eaw

This SN is the one object in our sample that could vaguely be described as displaying a red colour of the order of our model predictions. As such, we afford this object some further discussion.

The progenitor underwent a modest increase in brightness of 20 per cent at 4.5 μm, around 3 yr before SN. Meanwhile, it remained stable at 3.6 μm (Kilpatrick & Foley 2018; Rui et al. 2019; Van Dyk et al. 2019), and displayed no detectable variability in these bands in the 50–500 d before explosion. It showed little evidence of variability at I for the 12 yr preceding explosion. Finally, Johnson, Kochanek &

[4]We chose the $R-I$ colour for this study as it leads to the largest homogeneous sample of progenitors. There are a small number of progenitors with additional pre-explosion detections or limits in the *V*-band, but these data do not add anything conclusive to the discussion here.

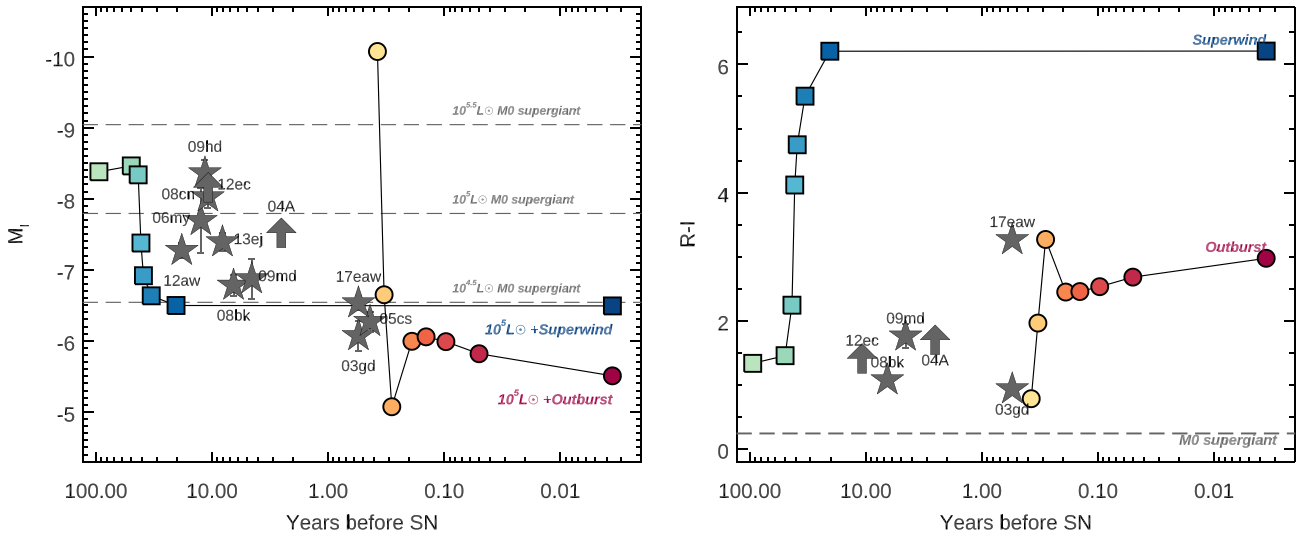

Figure 7. The *I*-band magnitude (left-hand panel) and $R-I$ colour (right-hand panel) as a function of time for each scenario tested. On each panel, we overplot observations of SN progenitors, taking data from Davies & Beasor (2018), Davies & Beasor (2020), and references therein. We also overplot the location of an RSG of spectral type M0 for three different luminosities.

Adams (2018) claimed that the progenitor's flux was stable to within ±0.4 per cent in the *R*-band across multiple observations between 0.5–9 yr. However, these authors also point out that they do not detect the progenitor in any individual observation, therefore we treat this evidence with caution.

Each of Kilpatrick & Foley (2018), Van Dyk et al. (2019), and Rui et al. (2019) argue for a very cool effective temperature *and* substantial circumstellar dust, based on the progenitor's spectral energy distribution. Specifically, the progenitor was redder at $R-I$ and brighter at 4.5 μm than is expected from standard PHOENIX or MARCS models; a phenomenon that both works attributed to dust. However, it was shown in Davies & Plez (2021) that attaching a modest wind to a 3800-K (= M0) model atmosphere can adequately explain this behaviour. At mass-loss rates of $0.3-1.0\times10^{-5}\,\mathrm{M_\odot\,yr^{-1}}$, the wind increases the TiO absorption mimicking a much later spectral type and a redder $R-I$, whilst pushing the CO bands at $\gtrsim$4 μm into emission to reproduce the observed increase in flux at 4.5 μm.

Taking the above into account, we conclude that SN 2017eaw did *not* undergo an outburst or a superwind-like event prior to exploding. Rather, the red pre-explosion colour and mild brightening at 4.5 μm are instead better explained by a modest increase in mass-loss rate to around $\sim10^{-5}\,\mathrm{M_\odot\,yr^{-1}}$; several orders of magnitude shy of being enough to generate $\sim0.1\,\mathrm{M_\odot}$ of CSM by the time of SN. Of course, we cannot exclude that the progenitor underwent some further, more substantial variability in the ∼6 months between the final progenitor observations and the SN.

4.2 Possibility of sample biases

Finally, we discuss the possibility that the local sample of SNe used here to critique the predictions of each scenario is biased with respect to those works which claim near-ubiquity for greatly elevated CSM densities at the point of explosion; specifically those of M18 and F18.

The objects in F18 are from a magnitude limited survey, in that the sample contains all II-P SNe that were detected during an observing campaign. Though systematic, the F18 sample is likely biased towards brighter SNe. The sample of SNe in M18 on the other hand is more heterogeneous, in that the data for these objects were taken from the literature, and chosen for their well-sampled light curves in terms of both time and multiband coverage. Finally, the data we present to compare to the synthetic spectra of the two scenarios are nominally volume limited, though there is potentially a bias towards SNe in bright (and therefore metal rich) galaxies which are more likely to have archival *HST* observations.

Despite their contrasting approaches to drawing their samples, each of the M18 and F18 studies concluded the same: that the majority of II-P light curves are consistent with $\gtrsim0.1\,\mathrm{M_\odot}$ of CSM at the point of explosion (13/20 and 35/37 objects for M18 and F18, respectively). Therefore, no matter how the sample of SNe is compiled, the results are qualitatively the same: most II-P SNe display evidence of atypically large amounts of CSM at explosion, irrespective of how the sample is compiled.

Furthermore, we can check that our SN progenitor sample is not biased with respect to the M18 sample since there are several objects in common. Specifically, four SNe from M18 (05cs, 12aw, 12ec, 13ej) have progenitor detections in the *I*-band. Three out of these four were determined to have $\gtrsim0.2\,\mathrm{M_\odot}$ of CSM at explosion (the exception being 05cs, which according to M18 had $<0.03\,\mathrm{M_\odot}$). Despite this, the pre-explosion brightnesses of these three SN were all consistent with an unobscured progenitor with $L\sim10^5\,\mathrm{L_\odot}$.[5] Though the number of overlapping objects is small, we conclude that the apparently 'normal' brightness and colours of the observed progenitors with respect to the predictions of the 'superwind' scenario is unlikely to be an artefact of sample biases.

5 CONCLUSIONS

Several recent studies in the literature have claimed that abnormally dense CSM is almost always present around RSGs at the point of collapse. In this paper, we have tested two scenarios under which such large amounts of CSM may be generated: a short 'outburst'

[5]Unfortunately, only one of these progenitors (12ec) has pre-explosion imaging in the *R*-band, in which the object is not detected, with an upper limit that has little diagnostic power.

lasting less than a year, with a mass-loss rate of $\dot{M} \gtrsim 0.1\,\mathrm{M}_{\odot}\,\mathrm{yr}^{-1}$; and an extended 'superwind' phase with $\dot{M} \sim 10^{-3}\,\mathrm{M}_{\odot}\,\mathrm{yr}^{-1}$ lasting $\sim$100 yr. Our conclusions may be summarized as follows:

(i) Each scenario creates large amounts of optically thick circumstellar gas, which attenuates the flux in the optical by several orders of magnitude. This means that an RSG on the verge of core-collapse would be very red and very faint in the optical, regardless of how or on what time-scale the material was produced.

(ii) The much slower build-up of CSM within the 'superwind' scenario causes the progenitor to be conspicuously red and faint for many decades preceding SN. This is strongly inconsistent with observations of nearby SNe, which have always appeared to have colours and magnitudes normal for mid- to late-M supergiants.

(iii) Therefore, whatever the mechanism for generating this CSM, it must do it on a very rapid time-scale. Specifically, the build-up of the CSM must happen within a year of the core-collapse.

The final overarching conclusion we can make from this work is that, shortly before core-collapse, RSGs must undergo some prodigious mass-losing event which radically alters the appearance of the star. Therefore, the signature of an imminent explosion should be a dramatic change in the progenitor stars' optical – near-IR photometry on time-scales of less than a month. Such a signature should be detectable in the coming era of wide-field short cadence photometry.

ACKNOWLEDGEMENTS

We thank Viktoriya Morozova for providing the models for the 'outburst' scenario, and for discussions during the course of this work. We also thank Emma Beasor and Nathan Smith for useful discussions, and the anonymous referee who's careful review helped us improve the paper.

DATA AVAILABILITY

The synthetic spectra generated as part of this study are available on request to the authors.

REFERENCES

Beasor E. R., Davies B., 2018, MNRAS, 475, 55
Beasor E. R., Davies B., Smith N., van Loon J. T., Gehrz R. D., Figer D. F., 2020, MNRAS, 492, 5994
Bruch R. J. et al., 2021, ApJ, 912, 46
Davies B., Beasor E. R., 2018, MNRAS, 474, 2116
Davies B., Beasor E. R., 2020, MNRAS, 493, 468
Davies B., Plez B., 2021, MNRAS, 508, 5757
Davies B., Origlia L., Kudritzki R., Figer D. F., Rich R. M., Najarro F., Negueruela I., Clark J. S., 2009, ApJ, 696, 2014
Dessart L., John Hillier D., Audit E., 2017, A&A, 605, A83
Förster F. et al., 2018, Nature Astron., 2, 808 (F18)
Goldman S. R. et al., 2017, MNRAS, 465, 403
Harper G. M., Brown A., Lim J., 2001, ApJ, 551, 1073
Humphreys R. M., Helmel G., Jones T. J., Gordon M. S., 2020, AJ, 160, 145
Jacobson-Galán W. V. et al., 2022, ApJ, 924, 15
Johnson S. A., Kochanek C. S., Adams S. M., 2018, MNRAS, 480, 1696
Khazov D. et al., 2016, ApJ, 818, 3
Kilpatrick C. D., Foley R. J., 2018, MNRAS, 481, 2536
Kochanek C. S. et al., 2017, MNRAS, 467, 3347
Moriya T. J., Yoon S.-C., Gräfener G., Blinnikov S. I., 2017, MNRAS, 469, L108
Morozova V., Piro A. L., Renzo M., Ott C. D., 2016, ApJ, 829, 109
Morozova V., Piro A. L., Valenti S., 2017, ApJ, 838, 28
Morozova V., Piro A. L., Valenti S., 2018, ApJ, 858, 15 (M18)
Morozova V., Piro A. L., Fuller J., Van Dyk S. D., 2020, ApJ, 891, L32 (M20)
Plez B., 2012, Astrophysics Source Code Library, record ascl: 5004
Rui L. et al., 2019, MNRAS, 485, 1990
Shenoy D. et al., 2016, AJ, 151, 51
Smartt S. J., 2015, PASA, 32, e016
Smartt S. J., Maund J. R., Hendry M. A., Tout C. A., Gilmore G. F., Mattila S., Benn C. R., 2004, Science, 303, 499
Smartt S. J., Eldridge J. J., Crockett R. M., Maund J. R., 2009, MNRAS, 395, 1409
Sukhbold T., Woosley S. E., Heger A., 2018, ApJ, 860, 93
Van Dyk S. D. et al., 2019, ApJ, 875, 136
Yaron O. et al., 2017, Nature Phys., 13, 510

This paper has been typeset from a TEX/LATEX file prepared by the author.